

Study of the early phase of a Coronal Mass Ejection driven shock in EUV images

Federica Frassati^{1,2} · Roberto Susino¹ · Salvatore Mancuso¹ · Alessandro Bemporad¹

Received: 24 December 2016 / Accepted: 13 September 2017 / Published online: 20 September 2017
© Springer Science+Business Media B.V. 2017

Abstract The November 1st, 2014 prominence eruption (associated with a C2.7 class flare) resulted in a fast, partial-halo Coronal Mass Ejection (CME). During its early propagation, the CME produced a type II radio burst (seen by the Bruny Island Radio Spectrometer) starting around 04:57 UT when the front entered into the LASCO/C2 field of view (FOV) and the top of the CME front was at the heliocentric distance of about $2.5 R_{\odot}$. In order to identify the source of the type II radio burst, we studied the kinematic of the eruption with EUV images acquired by SDO/AIA. Profiles of the observed EUV front speed have been compared with the Alfvén speed profiles derived by combining the plasma electron densities obtained from Emission Measure analysis and model magnetic fields extrapolated on the plane of the sky. Our results show that the northern half of the front became super-Alfvénic at approximately the same time when the type-II radio burst started. A comparison between the starting frequency of the type II emission and the frequencies corresponding to the coronal densities of the locations where the EUV front became super-Alfvénic suggests that the radio sources should be located in the northern flank of the front.

Keywords Sun: (CMEs) · Shocks · Electron density

1 Introduction

Coronal Mass Ejections (CMEs) can be defined as expulsions of huge quantities of chromospheric and coronal plasma propagating from the Sun into the heliosphere. They are associated with various solar phenomena (e.g., flares, eruptive prominences, shocks, EUV waves), although inter-relationships among them are not fully understood as yet.

The early evolution of CMEs is often impulsive and their expansion can occur at quite large velocities (up to 2000 km s^{-1} , Gopalswamy et al. 2014). If a CME is faster than the magnetosonic speed of the ambient medium, it can drive a shock where the electrons can be accelerated to near-relativistic energies to produce type II radio emission in low-frequency dynamic spectra (Mancuso and Raymond 2004; Vršnak and Cliver 2008; Carley et al. 2013).

Over the last decades a great deal of information on the shock speed and the density compression ratio across the shock can be also derived from White Light (WL) coronagraphic data (Vourlidas et al. 2003; Ontiveros and Vourlidas 2009; Bemporad and Mancuso 2011).

CMEs and associated shocks can be recognized in WL images as bright emission feature outwardly expanding into the interplanetary space with their lower part connected to the Sun. This kind of data will be used in a further development of this work.

Over the last few years full-disk observations in the EUV using the Atmospheric Imaging Assembly (AIA) instrument (Lemen et al. 2012) onboard the Solar Dynamics Observatory (SDO) have allowed to study low coronal evolution of these events thanks to its high cadence, sensitivity and spatial resolution. In particular, the 193 \AA and 211 \AA bands of AIA usually provide better contrast for the detection of shock waves in the lower corona, and images acquired with these filters have already been used in many previous similar

✉ F. Frassati
frassati@oato.inaf.it

¹ INAF-Osservatorio Astrofisico di Torino, Strada Osservatorio 20, Pino Torinese (TO), Turin, Italy

² Facoltà di Fisica, Università degli Studi di Torino, Via Pietro Giuria 1, Turin, Italy

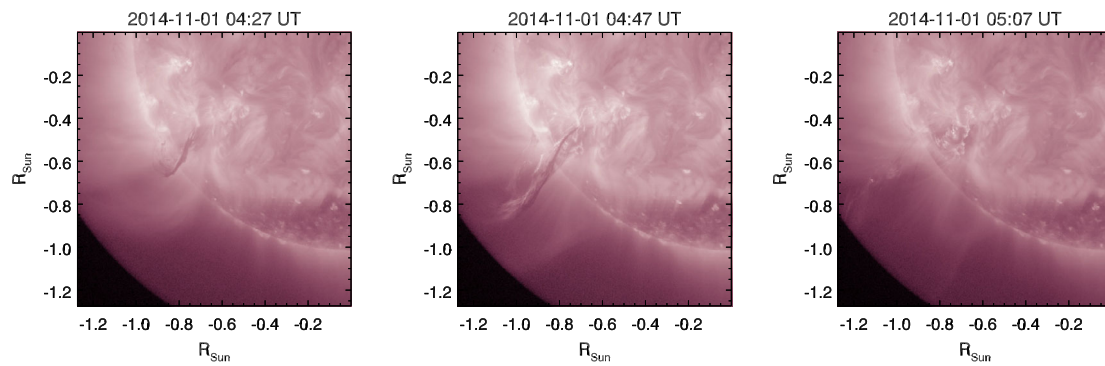


Fig. 1 SDO/AIA images of prominence eruption at 04:27–05:07 UT with 211 Å (Fe XIV) bandpass filter

studies (e.g. Zucca et al. 2014; Kouloumvakos et al. 2014; Kozarev et al. 2011).

When simultaneous radioheliograph observations are not available, it is possible to relate the emission of type II radio bursts to their heights with respect to the surface of the Sun but, in order to do that, it is necessary to provide a reliable estimate of the coronal electron density and Alfvén speed of the local corona. Empirical coronal electron-density models, derived with different techniques, have been often used in the literature to infer the shock height and kinematics from type II radio spectra, and, in turn, to study the CME kinematics, such as those provided by Newkirk (1961), Saito et al. (1977) and Mann et al. (1999). The use of these reference density models has the advantage that results obtained by authors for different events can be directly compared to each other. Unfortunately, however, they probably do not represent the actual density through which the eruption passes.

An alternative method to derive the CME/shock kinematics can be directly inferred from sequences of EUV and WL observations of off-limb CME events. The CME speed can be thus compared with the Alfvén speed in order to determine the time and altitude where the expanding EUV front becomes super-Alfvénic; this can be done once the electron density for the actual corona being crossed by the eruption is derived and by assuming values for the extrapolated coronal magnetic field. In what follows, we describe the November 1st, 2014 eruption and the analysis technique applied to SDO/AIA data together with our results.

2 Observations

On 2014 November 1st, a prominence eruption was observed by the multi-filter AIA instrument. Figure 1 shows three consecutive images acquired with the 211 Å (Fe XIV) bandpass filter. The eruption was associated with a long duration C2.7 class flare starting around 04:44 UT and ending at 07:05 UT as observed by the GOES-15 satellite originating in the source region located at 22°S and 52°E (Fig. 2),

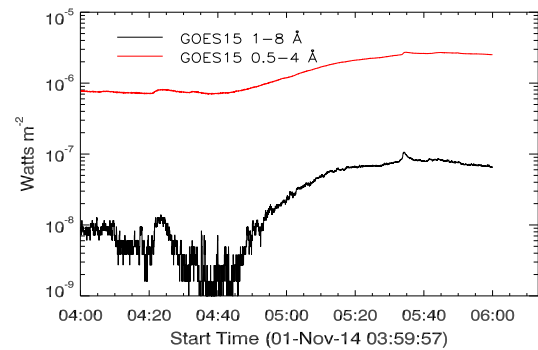


Fig. 2 GOES-15 soft X-ray flux measured on 2011 November 14. The flare onset is around 04:44 UT

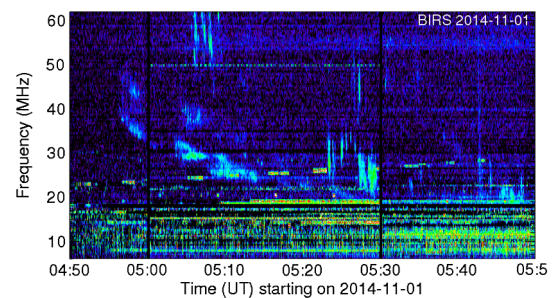


Fig. 3 Radio dynamic spectrum of the type II radio burst recorded by the BIRS station. The slowly drifting features starting at about 04:57 UT mark the presence of a coronal shock moving upwards in the corona through a decreasing density

not classified by NOAA. This was a ‘spotless’ flare (a flare occurring far from any active sunspot region) and resulted in a fast (leading edge speed of $\sim 1600 \text{ km s}^{-1}$), partial-halo (angular width of $\sim 160^\circ$) CME. The eruption was associated with a type II radio burst (Fig. 3) as detected by the Bruny Island Radio Spectrometer (BIRS) (Erickson 1997), starting around 04:57 UT, when the CME leading edge entered into LASCO/C2 field of view (FOV) above $2.2 R_\odot$. The fundamental harmonic was calculated from the radio burst trace (assuming that the emission observed by BIRS is from the second harmonic), with starting frequen-

cies of ~ 37 MHz (~ 74 MHz for the second harmonic). In what follows these frequencies will be compared with the coronal plasma frequencies encountered by the expanding EUV front, and the front speeds will be compared with local Alfvén speeds at different inclination angles, in order to derive information on the possible location of the radio burst emission.

3 Method and data analysis

3.1 Pre-CME electron density

In order to identify the coronal regions where the front speed exceeded the local Alfvén speed, our first step is the derivation of pre-CME coronal electron density n_e on the plane of the sky (POS). This was obtained by using the method developed by Aschwanden et al. (2013) in which the Differential Emission Measure (DEM), representing the amount of the emitting material as a function of coronal plasma temperature along the line of sight (LOS), is calculated by using six SDO/AIA filter images (94-131-171-194-211-335 Å). The authors assumed Gaussian profiles as representations of the DEM, which is characterized by Emission Measure (EM), Temperature T and the logarithmic Gaussian temperature width σ in each pixel position. By integrating the DEM curves pixel by pixel over the range of temperatures covered by SDO/AIA filters (0.5–20 MK), the Emission Measure is obtained as a function of heliocentric distance r and latitude ϕ :

$$EM(r, \phi) = \int \frac{dEM(r, \phi, T)}{dT} dT \quad [\text{cm}^{-5}] \quad (1)$$

that can be written as

$$EM(r, \phi) \simeq \int n_e^2 ds \quad [\text{cm}^{-5}] \quad (2)$$

Knowing the extension along the LOS of the plasma emission region, $s(r)$, and inverting Eq. (2), the electron density can be obtained as

$$n_e(r, \phi) \simeq \sqrt{\frac{EM(r, \phi)}{s(r)}} \quad [\text{cm}^{-3}] \quad (3)$$

We calculated the effective LOS path length in the same way used in the study of stellar atmospheres (Menzel 1936):

$$s \sim (H\pi r)^{1/2} \quad [\text{cm}], \quad H = \frac{k_B T}{\mu m_p g} \quad [\text{cm}] \quad (4)$$

where H is the hydrostatic scale height, T is the coronal temperature (equal for protons and electrons, by assuming thermal equilibrium), k_B is the Boltzmann’s constant, $\mu = 0.61$ is the mean molecular weight and g is the gravitational acceleration at the solar surface; we chose a constant value $T = 2 \cdot 10^6$ K as typical coronal temperature (as previously done also by Zucca et al. 2014). The electron density

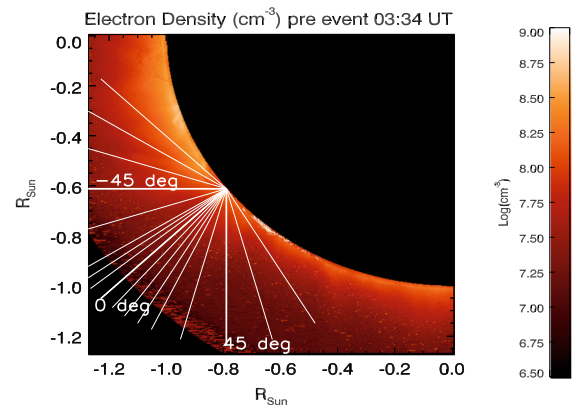


Fig. 4 2D map of the electron-density in the region of interest involved in the early CME propagation at 03:34 UT. The white lines represent the directions selected to study the eruption

has been derived by analysing a sequence of AIA frames acquired at 03:34 UT, before the beginning of the prominence rising phase. Figure 4 shows the electron-density 2D map of the region of interest considered in this work.

3.2 Pre-CME magnetic fields

The second step for estimating the Alfvén speed of the ambient corona is the determination of coronal magnetic fields.

As of now, magnetic fields cannot be measured directly in the solar corona, hence we used a numerical model based on polytropic magnetohydrodynamic (MHD) simulations elaborated by the Predictive Science group (http://www.predsci.com/hmi/data_access.php) to predict the state of the corona.

The heliocentric distance range covered by the simulation goes from 1 to $30 R_\odot$.

The main steps that are necessary to build up this model are the following:

- The photospheric magnetic field data during the time of interest are used to specify the boundary condition on the radial magnetic field;
- The measured photospheric magnetic field, together with an assumed uniform density and temperature at the photosphere, is used to solve the steady state MHD equations in the corona;
- The three-dimensional simulation is finally carried out.

The extrapolation used in this work was provided for the Carrington Rotation CR2156 (starting on October 15, 2014). The computed magnetic field, given in spherical coordinates, was converted into Cartesian coordinates and extracted on the POS, as viewed from the Earth on November 1st 2014 at 04:00 UT.

3.3 Pre-CME Alfvén speed

Once the pre-CME coronal density and the magnetic field are known, the Alfvén speed v_A (i.e., the propagation speed of incompressible plasma waves parallel to the magnetic field) can be calculated as:

$$v_A = 10^{-5} \cdot \frac{B}{\sqrt{4\pi n \mu m_H}} \quad [\text{km s}^{-1}] \quad (5)$$

where B (Gauss) is the magnitude of magnetic field, m_H (g) is the hydrogen mass and $n \sim 1.92 \cdot n_e$ (cm^{-3}) is the plasma number density. To calculate the Alfvén speed, we used the electron density derived before the event at 03:34 UT, in order to be sure that the prominence had not erupted yet. In fact, the aim of this analysis is to derive the pre-CME Alfvén speed in the coronal region that is crossed later on by the expanding CME.

3.4 CME distance-time profiles

The EUV front associated with the CME and observed in the low corona with SDO/AIA is the most probable candidate for the excitation of the type II radio burst recorded by the BIRS radio spectrometer, starting around 04:57 UT.

In order to study the kinematics of the EUV expanding front, we used distance-time plots obtained from the 211 Å images to built off-limb distance-time plots for each different direction of the expanding EUV wave as a function of the distance d from the origin of the prominence eruption on the limb (as shown in Fig. 1 and Fig. 4). We extracted 17 distance-time profiles inclined at 17 different angles with respect to direction of expansion (as seen in all images acquired by SDO/AIA), going from -90° to $+75^\circ$ measured counter-clockwise.

In order to measure the speed of the EUV front, the highest expanding structure visible in EUV images was selected for every angular direction and followed over different frames in the distance-time plots. Two examples of these plots (angles of -10° and 0°) are given in Fig. 5, where the red points represent the location of the expanding EUV front. The distance-time profiles of the EUV front were then fitted with a first-order polynomial (representing the slow rising phase) followed by a second-order polynomial (representing the impulsive acceleration phase). The parameters obtained from the fit provide the speed v_{EUV} of the EUV front during its expansion. The uncertainties on the observed speeds were derived from the propagation of measure errors. In particular, we assumed an uncertainty of ± 10 pixels in the determination of the distance d , as a consequence of the visual inspection of AIA data necessary to track the CME features. From the fitting procedure we then obtained the 1σ errors on the fit parameters that were used to derive upper and lower limits for the front speed. The expansion speed resulting from the fit has been compared at different

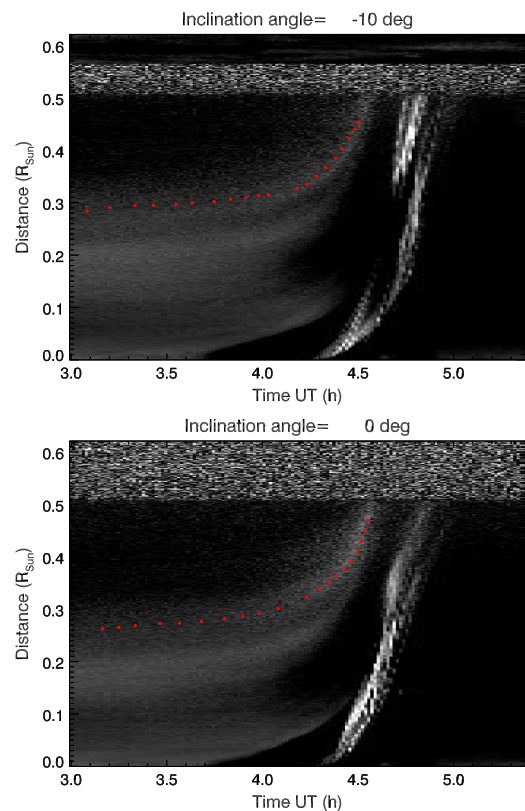


Fig. 5 The distance-time plot at -10° and 0° (see Fig. 4 for the orientation). To reconstruct the kinematic evolution of the EUV front we used a second order polynomial fit for the last ten points selected (right-side of plot)

times and distances with the local Alfvén speed in order to identify the locations where the EUV front became super-Alfvénic ($v_{EUV} > v_A$); this was done by extrapolating the fitting curves beyond the outer limit of the AIA FOV when necessary. The uncertainties on these locations were estimated considering the upper and lower limit curves for the front speed, as mentioned above.

4 Results

4.1 Comparison between front and Alfvén speeds at fixed distance

To study the geometry of the expanding front and investigate whether the expansion is spherically symmetric or not, we chose a fixed distance $d = 0.5 R_\odot$ from the origin of the prominence eruption on the limb for all different orientations sampled in our analysis. This is interesting because, the occurrence of an asymmetric expansion could indicate where the EUV front will expand faster, more likely exciting type-II radio bursts and maybe accelerating particles. Similar asymmetries have been found in EUV images of early

Table 1 The EUV front speed and the Alfvén speed measured at $0.5 R_{\odot}$ from the origin of the eruption obtained at different considered directions (see Fig. 4)

Angle (deg)	Speed (km s^{-1})	Alfvén Speed (km s^{-1})
-75	151 ± 9	260
-60	137 ± 15	237
-45	108 ± 13	271
-30	132 ± 8	338
-15	117 ± 10	361
-10	142 ± 8	347
-5	192 ± 12	350
0	185 ± 12	382
5	192 ± 13	394
10	188 ± 13	397
15	235 ± 10	405
20	246 ± 9	424
30	251 ± 11	414

solar eruption expansion phases for instance by Aparna and Tripathi (2016) and Zheng et al. (2011).

The corresponding front speeds are provided in Table 1. This reference distance was the largest in the SDO/AIA FOV for which we have measured values at all inclination angles. Note that we excluded radial profiles at inclination angles where it was not possible to follow the expanding front due the absence of an evident EUV signature. The Alfvén speed values extrapolated from the 2D maps (obtained as explained in Sect. 3.3) at $0.5 R_{\odot}$ along the same directions (see Sect. 3.3) are listed in the third column of Table 1 and are compared with the speeds derived from the observations.

As seen from Table 1, at the considered off-limb distance, the speed of the EUV front does not exceeds the Alfvén speed along the selected directions.

4.2 Comparison between front and Alfvén speed profiles

Since the EUV did not appear to become super-Alfvénic within the AIA FOV, we examined the evolution at larger distances by extrapolating the expansion speed curves (using the parameters derived from the second-order polynomial fit, see Sect. 3.4), and comparing them with the Alfvén speed profiles.

We calculated the Alfvén speed using the magnetic field values for the total magnetic field magnitude provided by Predictive Science and electron-density 2D maps (see Sects. 3.1 and 3.2). To this end, we fitted the unidimensional

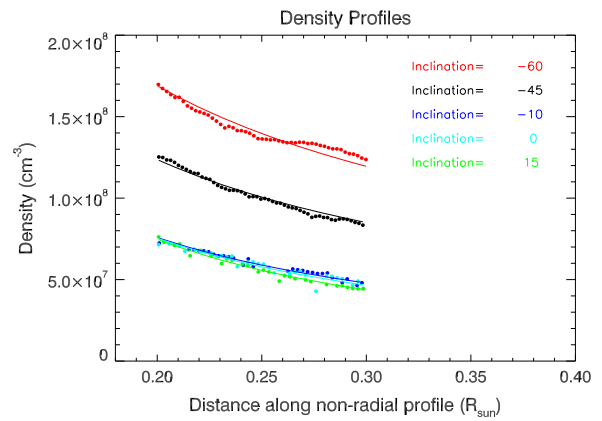


Fig. 6 Electron-density profiles (dots) observed at different inclination angles, as indicated in the legend, and the corresponding fitting curves (solid lines) reported vs. the distance from the centre of the prominence eruption

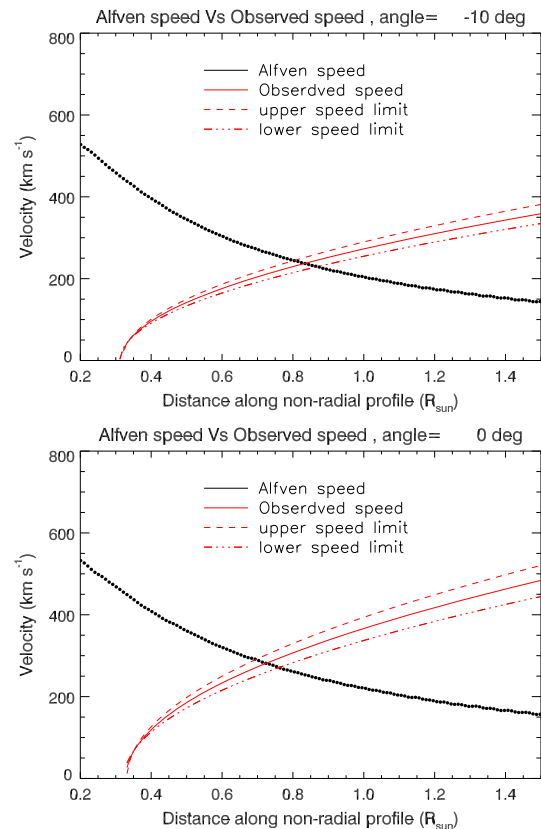


Fig. 7 Example: the Alfvén speed and front speed profiles observed at angles -10° and 0° . X axis shows the distance from the origin of the prominence eruption on the limb

profile of the electron-density using a power law function with two parameters:

$$n_e(d) = \frac{A}{\left(\frac{d}{R_{\odot}}\right)^B}, \quad d = \text{distance (km)} \tag{6}$$

Table 2 The table shows orientation angles, distances, times, plasma electron densities n_e and corresponding frequencies for the first (ν_{1st}) and second (ν_{2nd}) harmonics at locations where front speed exceeds Alfvén speed

Angle (deg)	Distance (R_\odot)	Time (UT)	n_e (cm^{-3})	ν_{1st} (MHz)	ν_{2nd} (MHz)
-75	0.61 ± 0.01	05 : 02 \pm 13	2.00×10^7	40.13	80.26
-60	0.65 ± 0.03	04 : 56 \pm 24	9.53×10^6	27.73	55.46
-45	0.77 ± 0.05	05 : 02 \pm 20	1.58×10^6	11.30	22.59
-30	0.85 ± 0.03	04 : 56 \pm 12	1.14×10^6	9.57	19.15
-15	0.87 ± 0.06	05 : 01 \pm 16	1.15×10^6	9.64	19.29
-10	0.83 ± 0.04	04 : 54 \pm 10	1.94×10^6	12.5	25.01
-5	0.67 ± 0.03	04 : 43 \pm 12	1.24×10^6	10.00	20.00
0	0.73 ± 0.03	04 : 47 \pm 13	1.396×10^6	10.57	21.14
5	0.75 ± 0.04	04 : 48 \pm 13	1.26×10^6	10.00	20.19
10	0.82 ± 0.05	04 : 52 \pm 14	0.59×10^6	6.88	13.75
15	0.71 ± 0.02	04 : 46 \pm 8	2.03×10^7	12.82	25.63
20	0.71 ± 0.02	04 : 47 \pm 9	0.30×10^6	4.89	9.78
30	0.69 ± 0.02	04 : 49 \pm 11	1.36×10^6	10.45	20.92

Table 3 The table shows orientation angles, distances, plasma electron densities n_e , the corresponding frequencies for the first (ν_{1st}) and second (ν_{2nd}) harmonics and Mach number at the on-set time of type-II radio burst (04:57 UT)

Angle (deg)	Distance (R_\odot)	n_e (cm^{-3})	ν_{1st} (MHz)	ν_{2nd} (MHz)	Mach number
-75	0.53 ± 0.04	1.73×10^7	37.32	74.64	0.7 ± 0.04
-60	0.66 ± 0.09	8.59×10^6	26.30	52.61	1.02 ± 0.13
-45	0.69 ± 0.15	3.46×10^6	16.71	33.42	0.83 ± 0.11
-30	0.87 ± 0.08	2.40×10^6	13.91	27.83	1.05 ± 0.08
-15	0.80 ± 0.12	3.31×10^6	16.34	32.68	0.87 ± 0.09
-10	0.88 ± 0.06	4.12×10^6	18.23	36.47	1.10 ± 0.07
-5	1.09 ± 0.02	1.53×10^6	11.12	22.25	2.25 ± 0.16
0	1.00 ± 0.04	2.10×10^6	13.02	26.04	1.70 ± 0.13
5	0.99 ± 0.04	1.97×10^6	12.59	25.18	1.53 ± 0.12
10	0.95 ± 0.07	1.29×10^6	10.18	20.37	1.23 ± 0.10
15	1.09 ± 0.02	2.13×10^6	13.12	26.24	1.87 ± 0.08
20	1.07 ± 0.02	0.21×10^6	4.16	8.32	1.82 ± 0.08
30	0.96 ± 0.03	1.36×10^6	10.46	20.92	1.62 ± 0.09

Examples of the extracted density profiles along several of the considered directions as well as the corresponding fitting functions, are plotted in Fig. 6. We show in Fig. 7 as example for the two directions with inclination angles of -10° and 0° .

To identify the locations where the shock was excited, we compared the local plasma frequency computed where the EUV front became super-Alfvénic with the starting frequency of type-II radio burst. The frequency ν_{1st} has been calculated as:

$$\nu_{1st} = 8980 \cdot \sqrt{n_e} \quad [\text{Hz}] \quad (7)$$

The results obtained are reported in Table 2 providing orientation angles, distances, times, plasma electron densities n_e and corresponding frequencies for the first (ν_{1st}) and second (ν_{2nd}) harmonics.

On the other hand, Table 3 provides the results obtained at the onset time of the type-II radio burst, in particular: front

distances, electron densities, corresponding plasma frequencies (for the first and second harmonics), and Mach numbers (ratios between the EUV front speeds and the Alfvén speeds) at that time for different inclinations.

The locations of points where the EUV front became super-Alfvénic at different times in the corona are shown in the left panel of Fig. 8 (left panel). These points were superposed into a PROBA2/SWAP frame (with a larger FOV than SDO/AIA) acquired just one minute before the type II radio burst starting time (04:57 UT). This figure suggests that the excitation of the type II radio burst could have been occurred, in principle, at quite different distances from the solar surface, depending on the considered inclination angle. Comparison between different frequencies and times listed in Table 2 and the observed starting frequency and time of the radio burst allowed us to identify its possible sources.

In particular, the middle panel of this figure shows that, on average, the shock formation occurred at a distance of

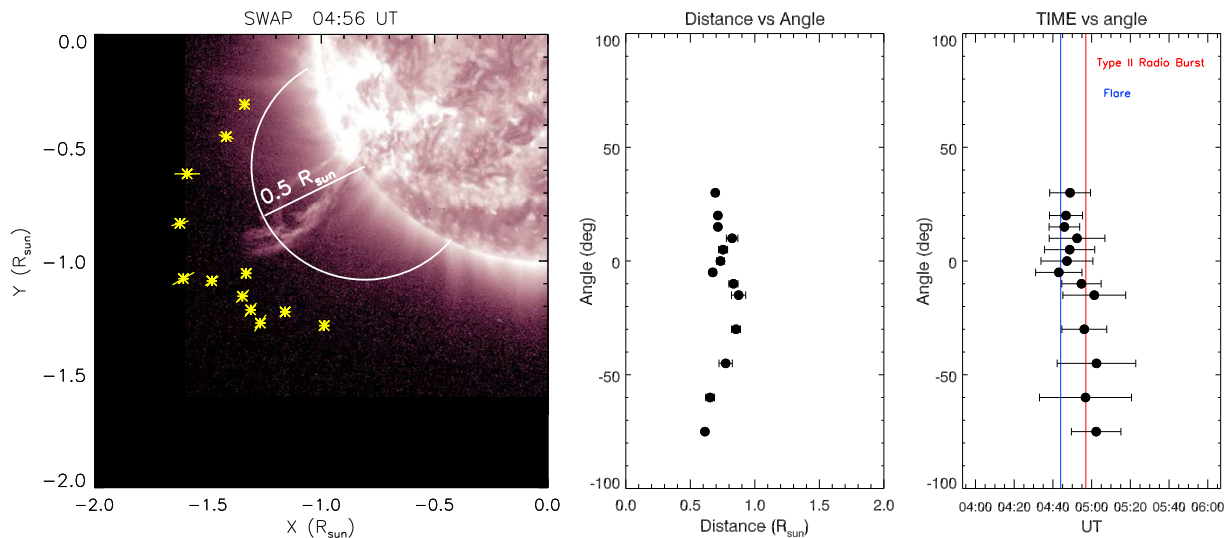


Fig. 8 *Left:* the yellow points (with errors bars) represent the locations where the EUV front becomes super-Alfvénic along the different directions considered. These points have been obtained by the intersection of extrapolated EUV front speeds and Alfvén speeds, as described in the text (see Fig. 5). *Middle:* relationship between the inclination angles

and the distances from the source of the eruption at which the extrapolated speeds exceed the Alfvén speed. *Right:* relationship between the inclination angles and times (compared also with flare and type-II radio burst times, vertical lines) at which the extrapolated speeds exceed the Alfvén speeds

$0.75 R_{\odot}$ from the source of the eruption and that in the northern part of the EUV front (negative inclination angles) the shock was likely excited at lower altitude.

Concerning the times at which the EUV front appeared to become super-Alfvénic, the points corresponding to the northern half (i.e., for inclination angles from -75° to -15°) seem to be systematically located around the type-II radio burst onset time (at 04:57 UT), as it can be seen from the time vs. angle plot shown in Fig. 8. Conversely, in the southern part the shock seems to be excited 8 minutes before (at 04:49 UT on average), a difference that is comparable with the average uncertainties.

Another interesting result in Table 2 is obtained from the comparison of the frequency of the first harmonic, ν_1 , calculated from the extrapolated electron density considering only northern flank of the front (-75° and -60°): the mean value is 38.2 MHz, not too different with respect to the starting frequency of the harmonic of type-II radio burst ($\nu_{burst} \simeq 37$ MHz).

On the other hand, Table 2 shows that the frequency for the first harmonic averaged over the Southern half (from -10° to 30°) of the front is much lower than ν_{burst} , thus suggesting that this part of the front is not responsible for the type-II radio emission. This suggests that the radio source was most likely located northward.

The same result is also supported by Table 3, showing that at the onset time of type-II radio burst the Northern half of the EUV front crossed a coronal region where the local plasma frequency was very close to the burst starting frequency.

5 Discussions and conclusions

In this work we presented a study of the early propagation of a EUV front occurred on 2014 November 1st, related with a prominence eruption, a fast CME and a C2.7 class flare. The presence of a type II radio burst is a clear signature of a shock excited over the field of view of SDO/AIA. Nevertheless, in general, if a magnetic flux-rope is expanding faster than the local magnetosonic or Alfvénic speeds, a shock should form, and this is true independently on the detection of a type II radio emission (Holman and Pesses 1983; Mann et al. 1995). Hence, in order to determine location and time of the shock formation, we focused on the kinematics of the front by using images acquired with the 211 Å (Fe XIV) bandpass filter of SDO/AIA, where the EUV features were observed with the best contrast.

We extracted unidimensional profiles in the plane of the sky, at different inclination angles with respect to the center of the rising prominence, in the time range between 03:00–05:30 UT. Then we collected all these profiles to build the distance-time maps that we fitted to derive the expansion speed of the EUV front. Using the estimated electron density and the extrapolated magnetic field we calculated the Alfvén speed along the same direction, and compared them with the EUV front speed. Our results show that the expanding front became super-Alfvénic in the northern half (from -75° to -15°) approximately at the same time of the type II radio burst onset time, in contrast with the southern half (which appeared to become super-Alfvénic about 8 minute before the type II emission).

Additional information could be derived from a comparison between the frequency of the radio emission and the plasma frequencies computed along the front based on the derived electron densities. In particular, the radio burst started with a frequency $\nu_{burst} \simeq 37$ MHz, corresponding to an electron density of about $n_{e,burst} \simeq 4.3 \times 10^6 \text{ cm}^{-3}$. Our results yield a value of 38.2 MHz averaged over the Northern flank of the front (-75° and -60°), not so bigger than the starting frequency of type-II emission measured by BIRS.

Considering that the front is propagating at all inclination angles towards lower densities, hence towards lower frequencies, Table 2 implies also that the southern half of the front was crossing regions with electron-plasma frequencies lower than the type-II starting frequency (37 MHz) already 8 minutes before, on average, the type-II burst starting time (04:57 UT). Hence, the southern half of the front did not cross the right frequencies, or densities, at the right time, opposite to what happened with the northern flank of the front.

The same result is also supported by Table 3, showing that at the onset time of type-II radio burst the Northern half of the EUV front crossed a coronal region where the local plasma frequency was very close to the burst starting frequency. Thus, we can conclude that the type II burst was excited most likely along the northern flank of the front. This is in qualitative agreement with the presence of nearby coronal loop structures, located northward of the eruption source region (as seen by the AIA images, Fig. 1) and of a faint North-East coronal streamer complex (as seen by the SOHO/LASCO-C2 coronagraph). Hence, the northward part of the EUV front was likely interacting with denser, nearby features in the lower corona, becoming the possible location for the type II radio burst.

Acknowledgements We are grateful to the SOHO, SDO and BIRS teams for making their data available to us. F.F. acknowledges support from INAF Ph.D grant. The authors acknowledge the anonymous Referee for very useful comments.

References

- Aparna, V., Tripathi, D.: *Astrophys. J.* **819**, 71 (2016). [1601.01620](#). doi:[10.3847/0004-637X/819/1/71](#)
- Aschwanden, M.J., Boerner, P., Malanushenko, A., Schrijver, C.J.: *Sol. Phys.* **283**, 5 (2013)
- Bemporad, A., Mancuso, S.: *Astrophys. J. Lett.* **739**, 64 (2011). [1108.3783](#)
- Carley, E.P., Long, D.M., Byrne, J.P., Zucca, P., Bloomfield, D.S., McCauley, J., Gallagher, P.T.: *Nat. Phys.* **9**, 811 (2013). [1406.0743](#)
- Erickson, W.C.: *Proc. Astron. Soc. Aust.* **14**, 278 (1997)
- Gopalswamy, N., Xie, H., Akiyama, S., Mäkelä, P.A., Yashiro, S.: *Earth Planets Space* **66**, 104 (2014). [1408.3617](#). doi:[10.1186/1880-5981-66-104](#)
- Holman, G.D., Pesses, M.E.: *Astrophys. J.* **267**, 837 (1983). doi:[10.1086/160918](#)
- Kouloumvakos, A., Patsourakos, S., Hillaris, A., Vourlidas, A., Preka-Papadema, P., Moussas, X., Caroubalos, C., Tsitsipis, P., Kontogeorgos, A.: *Sol. Phys.* **289**, 2123 (2014). [1311.5159](#)
- Kozarev, K.A., Korreck, K.E., Lobzin, V.V., Weber, M.A., Schwadron, N.A.: *Astrophys. J. Lett.* **733**, 25 (2011). [1406.2372](#)
- Lemen, J.R., Title, A.M., Akin, D.J., Boerner, P.F., Chou, C., Drake, J.F., Duncan, D.W., Edwards, C.G., Friedlaender, F.M., Heyman, G.F., Hurlburt, N.E., Katz, N.L., Kushner, G.D., Levay, M., Lindgren, R.W., Mathur, D.P., McFeaters, E.L., Mitchell, S., Rehse, R.A., Schrijver, C.J., Springer, L.A., Stern, R.A., Tarbell, T.D., Wuelsel, J.-P., Wolfson, C.J., Yanari, C., Bookbinder, J.A., Cheimets, P.N., Caldwell, D., Deluca, E.E., Gates, R., Golub, L., Park, S., Podgorski, W.A., Bush, R.I., Scherrer, P.H., Gummin, M.A., Smith, P., Auker, G., Jerram, P., Pool, P., Soufli, R., Windt, D.L., Beardsley, S., Clapp, M., Lang, J., Waltham, N.: *Sol. Phys.* **275**, 17 (2012)
- Mancuso, S., Raymond, J.C.: *Astron. Astrophys.* **413**, 363 (2004)
- Mann, G., Klassen, T., Aurass, H.: *Astron. Astrophys.* **295**, 775 (1995)
- Mann, G., Aurass, H., Klassen, A., Estel, C., Thompson, B.J.: In: Vial, J.-C., Kaldeich-Schü, B. (eds.) 8th SOHO Workshop: Plasma Dynamics and Diagnostics in the Solar Transition Region and Corona. ESA Special Publication, vol. 446, p. 477 (1999)
- Menzel, D.H.: *Circ. - Harv. Coll. Obs.* **417**, 1 (1936)
- Newkirk, G. Jr.: *Astrophys. J.* **133**, 983 (1961)
- Ontiveros, V., Vourlidas, A.: *Astrophys. J.* **693**, 267 (2009). [0811.3743](#)
- Saito, K., Poland, A.I., Munro, R.H.: *Sol. Phys.* **55**, 121 (1977)
- Vourlidas, A., Wu, S.T., Wang, A.H., Subramanian, P., Howard, R.A.: *Astrophys. J.* **598**, 1392 (2003). [astro-ph/0308367](#)
- Vršnak, B., Cliver, E.W.: *Sol. Phys.* **253**, 215 (2008)
- Zheng, R., Jiang, Y., Hong, J., Yang, J., Bi, Y., Yang, L., Yang, D.: *Astrophys. J. Lett.* **739**, 39 (2011). doi:[10.1088/2041-8205/739/2/L39](#)
- Zucca, P., Carley, E.P., Bloomfield, D.S., Gallagher, P.T.: *Astron. Astrophys.* **564**, 47 (2014). [1402.4051](#)